nature portfolio

https://doi.org/10.1038/s41586-021-03809-4

Supplementary information

High-fidelity laser-free universal control of trapped ion qubits

In the format provided by the authors and unedited

Supplementary Information: High-fidelity laser-free universal control of two trapped ion qubits

R. Srinivas[1,2,*], S. C. Burd[1,2], H. M. Knaack[1,2], R. T. Sutherland[3,4], A. Kwiatkowski[1,2], S. Glancy[1], E. Knill[1,5], D. J. Wineland[1,2,6] D. Leibfried[1], A. C. Wilson[1], D. T. C. Allcock[1,2,6], and D. H. Slichter[1,*].
[1]National Institute of Standards and Technology, Boulder, CO 80305, USA
[2]Department of Physics, University of Colorado, Boulder, CO 80309, USA
[3]Physics Division, Physical and Life Sciences, Lawrence Livermore National Laboratory, Livermore, CA 94550, USA
[4]Department of Electrical and Computer Engineering, Department of Physics and Astronomy, University of Texas at San Antonio, San Antonio, TX 78249, USA
[5]Center for Theory of Quantum Matter, University of Colorado, Boulder, Colorado 80309, USA
[6]Department of Physics, University of Oregon, Eugene, OR 97403, USA
[*]To whom correspondence should be addressed;
E-mail: raghavendra.srinivas@colorado.edu; daniel.slichter@nist.gov.

I. DETAILS OF EXPERIMENTAL SETUP

We operate in an externally applied magnetic field $|\vec{B}_0| = 21.3\,\mathrm{mT}$, where the qubit transition $|{\downarrow}\rangle \leftrightarrow |{\uparrow}\rangle$ has a magnetic field sensitivity of $\frac{\partial\omega_0}{\partial B}/2\pi = -19.7\,\mathrm{MHz/mT}$. The value of $|\vec{B}_0|$ was chosen to provide a first-order magnetic-field-insensitive qubit transition between the states $|{\downarrow'}\rangle \equiv {}^2S_{1/2}\,|F=3, m_F=1\rangle$ and $|{\uparrow'}\rangle \equiv {}^2S_{1/2}\,|F=2, m_F=1\rangle$, with a frequency of 1.686 GHz. Such field-insensitive qubits can have measured coherence times of many seconds[8] or even minutes[56]. When not performing entangling gates, we could map the populations in $|{\downarrow}\rangle$ and $|{\uparrow}\rangle$ into the states $|{\downarrow'}\rangle$ and $|{\uparrow'}\rangle$ using microwave control pulses, allowing the qubit state to be stored coherently for much longer times than is possible in the $\{|{\downarrow}\rangle, |{\uparrow}\rangle\}$ qubit.

We prepare the $|{\downarrow}\rangle$ state by optical pumping on the ${}^2S_{1/2} \leftrightarrow {}^2P_{3/2}$ transitions at 280 nm with σ^+ polarized light. During and after sideband cooling, further optical pumping pulses on these transitions are applied to repump population into $|{\downarrow}\rangle$. Qubit readout is performed by detecting fluorescence from the laser-driven $|{\downarrow}\rangle \leftrightarrow |{}^2P_{3/2}, F=4, m_F=4\rangle$ cycling transition. To reduce readout errors, we use microwave pulses to "shelve" the $|{\uparrow}\rangle$ state to the $|{}^2S_{1/2}, F=2, m_F=-1\rangle$ state, detuned by $\approx 1.6\,\mathrm{GHz}$ from $|{\downarrow}\rangle$, before applying the readout laser beam. Our readout can only distinguish the total number of ions fluorescing (0, 1, or 2), not the state of each individual ion. We produce an oscillating magnetic field gradient at $\omega_g = 2\pi \times 5\,\mathrm{MHz}$ with an amplitude of 152(15) T/m at the ion by applying currents of 0.8(1), 1.1(1), and 1.1(1) A on qubit control electrodes 1, 2, and 3 respectively, shown in Fig. 1. The relative amplitudes and phases of these currents are chosen to minimize residual magnetic fields at ω_g at the ion position[43]; in practice, this means that the current in electrode 2 is driven approximately 180 degrees out of phase with the currents in electrodes 1 and 3. These currents dissipate $\approx 100\,\mathrm{mW}$ total in the trap from resistive losses. The weaker currents used to generate the microwave-frequency magnetic fields dissipate $\approx 6\,\mathrm{mW}$ in the trap. Currents in qubit control electrode 1 on resonance with the qubit frequency are used for global single-qubit operations. Based on sequences of 200 repeated π pulses on the $|{\downarrow}\rangle \leftrightarrow |{\uparrow}\rangle$ transition using a single ion, the error per π pulse has an upper bound of approximately 10^{-4}. We generate the radiofrequency and microwave currents with high-speed digital-to-analog converters followed by commercially available amplifiers and filters, as described in Section II A.

To achieve the highest entangled state fidelities, the out-of-phase radial mode used for entangling operations is first cooled near its ground state with sideband transitions driven by the radiofrequency gradient and microwave tones, interleaved with optical repumping[31,57]. This motional mode is coupled weakly to the out-of-phase axial mode; thermal phonon occupation in the out-of-phase axial mode will cause dephasing of the motional mode used for entanglement[58,59]. To reduce this dephasing, we also cool the out-of-phase axial mode near its ground state. For this mode, we use laser-based Raman sideband transitions, as the trap geometry prevents direct laser-free sideband cooling of the axial modes.

II. FIELDS AND GRADIENTS FOR ENTANGLING INTERACTION

The entangling interaction relies on the gradient of a magnetic field $\vec{B}_g$ oscillating at ω_g, as well as a microwave magnetic field $\vec{B}_\mu$ with frequency components at $\tilde{\omega}_0 \pm \delta$ (see Fig. 1A). This latter field can be equivalently described as a microwave field at $\tilde{\omega}_0$ whose amplitude varies sinusoidally with time t as $\cos(\delta t)$. A full derivation of how the entangling interaction arises from these fields is given in Ref. 41. As shown in Eq. 1, the slowly-rotating terms generate the interaction

$$\hat{H}_I(t) = \hbar\Omega_g J_2 \left(\frac{4\Omega_\mu}{\delta}\right)(\hat{\sigma}_{z1} - \hat{\sigma}_{z2})(\hat{a}e^{i\Delta t} + \hat{a}^\dagger e^{-i\Delta t}). \tag{S1}$$

The quantity Ω_g characterizes the strength of the gradient at ω_g used in the entangling interaction and is given by

$$\Omega_g \equiv \frac{r_0[\nabla(\vec{B}_g \cdot \hat{r}_q)\cdot\hat{r}]}{4} \left.\frac{\partial\omega_0}{\partial B}\right|_{B=|\vec{B}_0|}, \tag{S2}$$

where $\hat{r}$ is a unit vector along the motional mode, $\hat{r}_q$ is a unit vector along the quantization axis defined by an external static bias magnetic field $\vec{B}_0$, and $\frac{\partial\omega_0}{\partial B}$ is the magnetic field sensitivity of the qubit transition frequency. For these experiments $|\vec{B}_0| \approx 21.3\,\mathrm{mT}$, and $\vec{B}_0$ is in the plane of the trap electrodes at an angle of 67.5° to the trap axis. The ground state extent of the ions' motional mode in the trap is $r_0 = \sqrt{\hbar/2M\omega_r}$, where ω_r is the motional mode frequency and M is the total mass of both ions. We use the expression in Eq. S2 to determine the strength of the magnetic field gradient from the entangling operation duration. For these experiments, we tune the mode alignment to be along the gradient by maximizing Ω_g experimentally[57]; the mode angles are similar to those specified in Ref. 60.

The microwave fields are characterized by the corresponding resonant Rabi frequency

$$\Omega_\mu \equiv \frac{B_x}{2\hbar}\langle\downarrow|\hat{\mu}_x|\uparrow\rangle, \tag{S3}$$

where B_x is the component of the oscillating microwave magnetic field $\vec{B}_\mu$ perpendicular to the quantization axis and $\hat{\mu}_x$ is the magnetic moment of the ion in the same direction.

We can decompose $\vec{B}_g$ into $\vec{B}_{g,\parallel} + \vec{B}_{g,\perp}$, where $\vec{B}_{g,\parallel} \equiv (\vec{B}_g \cdot \hat{r}_q)\hat{r}_q$ is the component of $\vec{B}_g$ along the quantization axis and $\vec{B}_{g,\perp}$ is the component perpendicular to the quantization axis. To maximize the entangling interaction strength and reduce the modulation of the qubit frequency[43], we null $\vec{B}_{g,\parallel}$ at the ion positions by adjusting the relative phases and amplitudes of the currents at ω_g in all three qubit control electrodes. However, $\vec{B}_{g,\perp}$ is not simultaneously nulled and gives rise to an ac Zeeman shift Δ_{ac} on the qubit frequency [43]. We have $\Delta_{ac}/2\pi \approx -400\,\mathrm{kHz}$ for the configuration of currents at ω_g used in the entangling operation. The qubit frequency in the absence of any control fields at ω_g is ω_0. With the control fields at ω_g, the qubit frequency is shifted to $\tilde{\omega}_0$, where $\tilde{\omega}_0 = \omega_0 + \Delta_{ac}$.

Like $\vec{B}_{g,\parallel}$, $\vec{B}_{g,\perp}$ has a spatial gradient, which means Δ_{ac} likewise has a spatial gradient. If the ion crystal is rotated relative to the trap axis, the two ions will experience different values of $\vec{B}_{g,\perp}$ and thus different ac Zeeman shifts, which we describe in terms of the average shift Δ_{ac} on both ions and the differential shift δ_{ac} between the two ions. We use this differential shift δ_{ac} for individual addressing in frequency space. In practice, we can achieve $\delta_{ac}/2\pi \approx 20\,\mathrm{kHz}$, with $\Delta_{ac}/2\pi \approx 2.5\,\mathrm{MHz}$, by driving a current at ω_g through only electrode 1. In this single-electrode driving configuration, $\vec{B}_{g,\parallel}$ is not nulled, but this is not necessary during the individual addressing operation. Choosing not to null $\vec{B}_{g,\parallel}$ allows higher values of δ_{ac} to be achieved.

A. Radiofrequency and microwave drive electronics

A schematic of the radiofrequency and microwave electronics used to generate the control fields is shown in Fig. S1. The signals at $\omega_g/2\pi = 5\,\mathrm{MHz}$ in the qubit control electrodes are generated by three independent 16-bit digital-to-analog converters (DACs), one per electrode, operating at 100 MS/s. The waveform frequencies, phases, and time-dependent amplitude envelopes are defined digitally, and then the waveforms are directly synthesized without subsequent analog modulation components. The DAC chips are on a common circuit board and have a shared clock to ensure a deterministic phase relationship between the signals in all three qubit control electrodes[61]. The DAC outputs are each low-pass-filtered, amplified to roughly 2 W per electrode, band-pass-filtered to remove harmonics and low-frequency noise, and sent to the low-frequency port of a custom resonant diplexer circuit (one per qubit control electrode) shown in Fig. S1b. The diplexers provide narrowband impedance transformation for the tones at ω_g, increasing the current in the trap electrodes for a given drive power by roughly a factor of 3 while reducing back-reflection to the amplifiers and providing additional bandpass filtering. The diplexers also serve to combine the tones at ω_g with the microwave tones near ω_0 onto the same trap electrodes. In practice, while tones at ω_g are used on all three electrodes, the microwave tones are only applied to one electrode (see Section II B for details). Most of the drive power at ω_g is dissipated in the resistive parts of the diplexer circuits; only about 100 mW of the $\approx$ 6 W of total drive power among all three electrodes is dissipated in the trap, due to resistive losses. Improvements to the resonant diplexer circuit design could provide increased currents at ω_g in the trap, and thus faster entangling interactions, with the same or smaller drive power. The qubit control electrodes are shorted to ground at the far end of the trap, approximately 3 mm away from where the ions are confined, producing a standing wave with a current antinode near the ion location. This doubles the current in the qubit control electrodes for a given drive power relative to using a 50 Ω termination and shifts most dissipation of the control signals to the impedance matching circuits and circulator terminations outside the vacuum system.

The microwave signals near $\omega_0/2\pi \approx 1.326$ GHz are

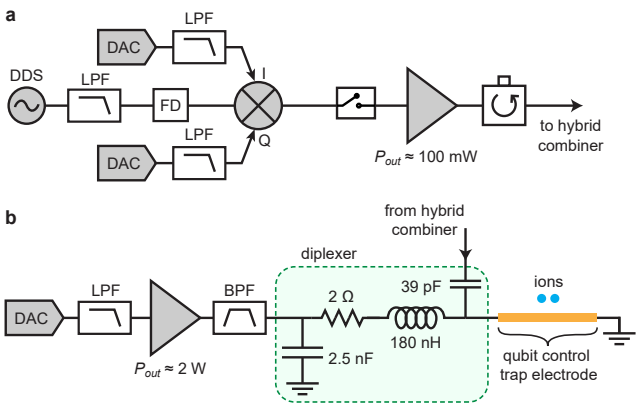

FIG. S1. **Drive electronics for qubit control fields. a,** Schematic of the microwave signal generation chain for a single frequency. Two such chains are used, one operating at $\tilde{\omega}_0 + \delta$ and the other at $\tilde{\omega}_0 - \delta$, and their outputs are combined using a microwave hybrid. **b,** Schematic of the circuit used for generating radiofrequency control signals at ω_g, combining them with the microwave signals, and delivering both to the trap. The circuit shown is for a single trap electrode; two duplicate circuits drive the other two qubit control trap electrodes, each with a different phase and amplitude of the drive at ω_g. However, microwave signals are only sent to the trap on one of the three electrodes. Abbreviations: LPF low-pass filter, BPF band-pass filter, FD frequency doubler, P_{out} amplifier output power.

generated by a pair of high-speed direct digital synthesizer (DDS) chips clocked at 2.4 GS/s. The DDS chips have a shared clock and are phase-synchronized to each other as well as to the DACs that generate the signals at ω_g. We filter, frequency-double, and amplify the DDS outputs, then use an IQ modulator on each channel to shape the amplitude envelope in time. The I and Q ports of the modulator are driven by low-pass-filtered DACs of the same design as those used to generate the signals at ω_g. The microwave signals then pass through a microwave switch to provide increased on/off ratio compared to the modulator alone, after which they are amplified to ~ 100 mW. The two tones are combined using a microwave hybrid and sent to one of the trap electrodes via the diplexer circuit described above, which combines them with the strong tone at ω_g for that electrode. A similar microwave chain, but without the IQ modulator, is used to generate rectangular microwave pulses at ω_0 for performing global single-qubit rotations, which are coupled onto the qubit control electrodes using a directional coupler between the hybrid coupler and the diplexer.

B. Entanglement pulse sequence

We show the pulse sequences used for the gradient and microwave fields used to generate our symmetric and antisymmetric entangled states in Fig. S2. The currents at ω_g and $\tilde{\omega}_0 \pm \delta$ are ramped up and down smoothly over 5 μs, with rising and falling edges following an approximate sine-squared envelope. Due to the size of the ac Zeeman shift Δ_{ac}, the drive at ω_g is ramped up completely before the microwave currents at $\tilde{\omega}_0 \pm \delta$ are ramped up, and the downward ramps are carried out in reverse order. The $\pi/2$ and π pulses at ω_0 are carried out when all the other currents are turned off, so the qubit frequency is not ac-Zeeman-shifted and the qubit is not driven off-resonantly. The phases of these pulses, denoted with subscripts x and y, where y indicates a 90° phase shift with respect to x, are chosen to provide robustness to miscalibrations (overrotation or underrotation) in the π pulses.

The total duration of the entangling operation is 740 μs, of which the up and down ramps (during which relatively little entanglement is generated) consume 160 μs. Increased currents at ω_g would increase Ω_g and thus reduce the overall gate duration. Decreasing the durations of the ramps must be done with care, as shorter ramp durations can lead to increased off-resonant qubit transitions that reduce the fidelity of the entangling operation[41]. We tried both higher and lower orders of Walsh modulation, with the highest fidelity entangling operations obtained using the Walsh 7 sequence[57].

III. FIDELITY ANALYSIS

In this section, we describe the methods used for Bell state fidelity analysis, including the correction of state preparation and measurement (SPAM) errors.

A. Estimating SPAM errors

We use reference data to determine our state preparation and measurement (SPAM) errors. We repeatedly prepare the ions approximately in the $|\downarrow\downarrow\rangle$ state and measure the ion fluorescence, building a histogram of the number of photon counts observed during the detection period. We also perform the same experiment but with a microwave π pulse at ω_0 applied to the ions prior to measurement, taking multiple sets of about 18,500 measurements per state. These experiments give reference count histograms for two or zero ions fluorescing, respectively (two "bright" ions or two "dark" ions). These are approximately Poissonian-distributed but contain additional corrections due to off-resonant pumping of dark ions into the bright state ("repumping"), optical pumping of bright ions into the dark state due to imperfect closure of the cycling transition ("depumping"), and imperfect optical pumping in the state preparation process that leaves an ion in a state outside the $\{|\downarrow\rangle, |\uparrow\rangle\}$ manifold ("leakage")[57]. We use maximum likelihood (ML) to estimate the Poissonian mean count rates from bright and dark ions, as well as depumping, repumping and leakage rates. We use these rates to construct calculated reference distributions for the case of zero, one, and two ions fluorescing.

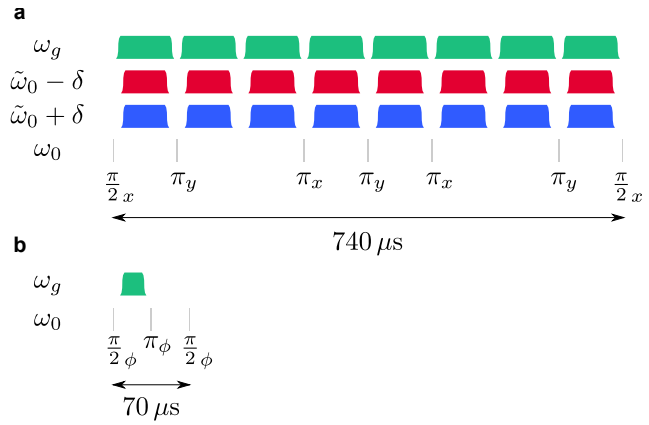

FIG. S2. **Pulse sequences for entangled state generation. a,** Pulse sequence for entangling interaction. We plot the amplitude of the control signals schematically versus time. The gradient oscillating at ω_g (green), as well as the two microwave fields symmetrically detuned by δ from the ac Zeeman shifted qubit frequency $\tilde{\omega}_0$ (red and blue), are ramped up and down eight times. Each of these eight sets of pulses nominally corresponds to a single closed loop in motional phase space; deviations from perfect loop closure are mitigated by Walsh modulation[42]. Additional $\pi/2$ and π pulses (gray) correct for qubit frequency offsets and drifts and perform the Walsh 7 modulation. These pulses are at ω_0, the qubit frequency unshifted by the ac Zeeman shift from the oscillating magnetic field at ω_g. The total duration of our entangling interaction is 740 μs. **b,** Pulse sequence for single ion addressing. This sequence is appended to the sequence in **a** to create the antisymmetric Bell state. We perform a spin-echo sequence, using the gradient oscillating at ω_g in only the first arm. The ac Zeeman shift from the magnetic field at ω_g imparts a phase rotation of π on the second qubit relative to the first. The phase of the global qubit rotation pulses in this sequence, here denoted by ϕ, must be calibrated relative to the entangling interaction in **a** to create the desired state $|\Psi_-\rangle$. The π pulse and second $\pi/2$ pulse have no effect on the state $|\Psi_-\rangle$; however, for a general initial state, the second $\pi/2$ pulse is necessary to perform the individually addressed spin flip, and the π pulse implements a spin echo to undo the effects of common-mode qubit frequency offsets.

We determine the probabilities P_0, P_1, and P_2 of zero, one, or two ions fluorescing, respectively, after an entangling operation using ML estimation based on the constructed reference distributions. According to tests using simulated count histogram data, the resulting state measurement error is at the $\approx 10^{-4}$ level or better for reference datasets of the size used in our fidelity analysis.

Using this technique, we determine the rate of state initialization errors due to leakage (note that this leakage occurs during preparation of the initial $|\downarrow\downarrow\rangle$ state, not during the entangling operation itself). Our reported fidelities are all corrected for this imperfection in state initialization, as described below. For the symmetric Bell state data, we determined a state initialization error rate per qubit due to leakage of $3.5(2) \times 10^{-3}$, while for the antisymmetric Bell state data, taken several weeks later, this rate was $1.7(2) \times 10^{-3}$. It is not possible using our analysis to distinguish between an ion incorrectly initialized in the $|\uparrow\rangle$ state and an error in the microwave π pulse; however, the data bound the combined rate of these two errors to be at or below $\approx 10^{-4}$ per qubit. We do not attempt to correct for either of these two types of errors, both of which would decrease the fidelity of the final entangled state.

B. Parity and population calculation

Each dataset consists of 40 sets each containing 200 repetitions of the entangling operation followed by population measurement ("population" trials) and 52 sets each containing 200 repetitions of the entangling operation followed by parity analysis pulses, with a different analysis phase for each set ("parity" trials). For the antisymmetric Bell states, we use 42 sets of 200 repetitions each as parity trials, composed of 7 sets at each of 6 evenly spaced phase values. We divide each dataset into "trigger" and "analysis" halves by assigning half of the population trials from each set (and for the antisymmetric Bell state, half of the parity trials from each set), chosen at random, to the "trigger" subset. For the symmetric Bell state, we assign every other set of 200 parity trials (versus analysis phase) to the "trigger" subset, rather than splitting each set of 200 in half. This choice improved the parity estimation based on analysis of simulated data. The random assignment algorithm is seeded by a hash of the unique dataset identifying number.

The fidelity of the final Bell state is determined from the populations and parity $(P_0 + P_2 - P_1)$ as described below. The populations are determined by combining all population trials into a single histogram and estimating P_0, P_1, and P_2 using maximum likelihood based on the reference distributions described above. The population measurements correspond to $P_0 + P_2$ and P_1 for the symmetric and antisymmetric states respectively.

To determine the amplitude of parity oscillations for the symmetric Bell state $|\Phi\rangle \equiv \frac{1}{\sqrt{2}}(|\downarrow\downarrow\rangle + i\,|\uparrow\uparrow\rangle)$, we maximize the joint likelihood over the count histograms for all the different analysis pulse phases, assuming a parameterized model of a sinusoidal parity oscillation versus phase and employing the reference count distributions described above. The ideal state $|\Phi\rangle$ will have a parity oscillation with amplitude 1. The symmetric state fidelity is the average of the population and parity oscillation amplitude.

For the antisymmetric Bell state $|\Psi_-\rangle = \frac{1}{\sqrt{2}}(|\downarrow\uparrow\rangle - |\uparrow\downarrow\rangle)$, the parity is determined by combining all parity trials into a single histogram and estimating P_0, P_1, and P_2 in the same way as described above. The parity for an ideal antisymmetric Bell state is -1, and is independent of the analysis $\pi/2$ pulse phase. The values of the parity analysis phases in this instance were chosen as multiples of $\pi/3$, such that the extracted parity using this method

would average over the amplitude of any parity oscillations due to residual population in a symmetric Bell state. The antisymmetric state fidelity is the average of the population and the negative of the parity. For both states, we then correct for the state initialization error as detailed in the next section.

C. Effects of initialization error

The density matrix describing the state of each ion $\rho_{0,1}$ after initialization is

$$\rho_{0,1} = (1-\epsilon)\left|\downarrow\right\rangle\left\langle\downarrow\right| + \epsilon\left|a\right\rangle\left\langle a\right|, \tag{S4}$$

where ϵ is the probability of producing the leaked state $|a\rangle$. The state $|a\rangle$ is outside of the qubit manifold and does not participate in the gate dynamics. This initialization error most likely occurs due to photon scattering from our Raman beams into the $|F=3, m_F=1\rangle$ state. This state does not fluoresce and is detected as dark through our detection process. We ignore any initialization in the $|\uparrow\rangle$ state, since our reference data indicate that this process is at least an order of magnitude less likely than producing the state $|a\rangle$. Furthermore, our reference data cannot distinguish preparation in the $|\uparrow\rangle$ state from an imperfect π pulse on the $|\downarrow\rangle \rightarrow |\uparrow\rangle$ transition. As any population in $|\uparrow\rangle$ state would only reduce the fidelity of the entangled state we measure, we do not correct for this error. For two ions, the initial density matrix is

$$\begin{aligned}\rho_{0,2} = (1-\epsilon)^2\left|\downarrow\downarrow\right\rangle\left\langle\downarrow\downarrow\right| + \epsilon(1-\epsilon)\big(\left|\downarrow a\right\rangle\left\langle\downarrow a\right| \\ + \left|a\downarrow\right\rangle\left\langle a\downarrow\right|\big) + \epsilon^2\left|aa\right\rangle\left\langle aa\right|.\end{aligned} \tag{S5}$$

We now analyze the effect of this initialization error on both the symmetric and antisymmetric entangled state fidelities.

1. Symmetric entangled state fidelity

Our entangling operation acts on a perfect $|\downarrow\downarrow\rangle$ input state to produce a symmetric entangled state $|\Phi\rangle \equiv \frac{1}{\sqrt{2}}(|\downarrow\downarrow\rangle + i\,|\uparrow\uparrow\rangle)$ with a fidelity F. The same operation acting on $|\downarrow a\rangle$ and $|a\downarrow\rangle$ instead flips the spin of the ion within the qubit manifold, resulting in $|\uparrow a\rangle$ and $|a\uparrow\rangle$ respectively, to first order. There will be higher-order terms that scale as $(1-F)\epsilon$, which we ignore. The entangling operation has no effect on the $|aa\rangle$ state. To determine the entangling operation fidelity F from the measured fidelity F_m, we must correct for the initialization error caused by leakage. We determine the fidelity F_m of our entangled state by measuring the ion populations after our entangling operation and the parity with an additional $\pi/2$ pulse with a variable phase[44]. The leaked states have no effect on the parity measurement, but will increase the measured populations as the leaked states are indistinguishable from $|\uparrow\uparrow\rangle$. Thus, F_m is

$$\begin{aligned}F_m &= (1-\epsilon)^2 F + \epsilon(1-\epsilon) + \frac{\epsilon^2}{2} \\ &= F - \epsilon(2F-1) + \epsilon^2(F-\frac{1}{2}) \\ &\approx F - \epsilon,\end{aligned} \tag{S6}$$

for $(1-F), \epsilon \ll 1$.

2. Antisymmetric entangled state fidelity

As with the symmetric state, we estimate the initialization-corrected fidelity F by making measurements of the populations after (ideally) generating the antisymmetric state $|\Psi_-\rangle = \frac{1}{\sqrt{2}}(|\downarrow\uparrow\rangle - |\uparrow\downarrow\rangle)$ and the parity with an additional $\pi/2$ pulse. Unlike the symmetric state, the ideal antisymmetric state has parity -1 for all phases. The parity for all other states is greater than -1. Thus, instead of trying to fit a low amplitude oscillation, we instead take the average parity from measurements with six different phases[57] of the $\pi/2$ pulse equally spaced in $[0, 2\pi)$. The symmetric state has 0 parity averaged over these phases..

For the leaked state, the single-ion addressing sequence, to first order, will transform $|\uparrow a\rangle \rightarrow |\downarrow a\rangle$ while leaving the $|a\uparrow\rangle$ state unchanged. The parity of these states after applying an additional $\pi/2$ pulse is 0, but these states will contribute to the population measurements. For the antisymmetric state, the measured fidelity F_m is related to F by

$$\begin{aligned}F_m &= (1-\epsilon)^2 F + \frac{\epsilon}{2}(1-\epsilon) \\ &= F - \epsilon(2F-\frac{1}{2}) + \epsilon^2(F-\frac{1}{2}) \\ &\approx F - \frac{3}{2}\epsilon,\end{aligned} \tag{S7}$$

again for $(1-F), \epsilon \ll 1$.

D. Bootstrap analysis

To generate the confidence intervals on our entangled state fidelities, we generate 5,000 synthetic ("bootstrapped") data sets by resampling the experimental photon count data for the entangled state analysis with replacement[62]. We also resample the corresponding reference data 5,000 times, each bootstrap having corresponding estimates of Poissonian means, depumping, repumping, and leakage. We construct the corresponding reference count distributions using additional variation of the Poissonian means, based on the magnitude of slow

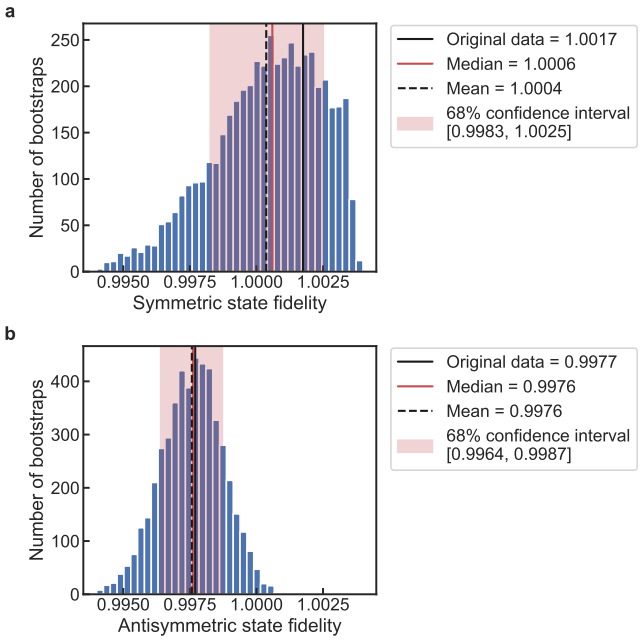

FIG. S3. **Distribution of bootstrapped fidelities.** We plot the distribution of bootstrapped fidelities for our symmetric (**a**) and antisymmetric entangled state data (**b**), which we use to determine the confidence intervals of Bell-state fidelities, corrected for state initialization errors. For each state, we resample the counts of the data with replacement 5000 times and reanalyze the data. For the means and 68% confidence intervals reported in the text, we truncate all fidelities at 1.

variations in these means seen experimentally over the course of a day. We then analyze each bootstrapped data set using a bootstrapped reference count distribution. The distributions of the resulting fidelities, corrected for preparation errors, for the triggered symmetric and antisymmetric Bell states are shown in Fig. S3a and b, respectively.

Due to statistical uncertainty in both the estimate of the uncorrected fidelity and the initialization error, our fidelity analysis method can give corrected fidelity estimates that exceed 1, which are nonphysical. When reporting fidelities, we therefore truncate any estimated fidelities greater than 1 at a value of 1. The lower and upper endpoints of our confidence intervals are the 16th and 84th percentile points of the distribution of bootstrapped fidelities, truncated to 1 as necessary. Note that the confidence interval for the symmetric state fidelity has both median and 84th percentile values of 1.

For the symmetric Bell state data, the estimated population is $1^{+0}_{-0.0011}$ and the parity amplitude is $0.9966^{+0.0019}_{-0.0064}$, with the uncertainties (68% confidence) determined from bootstrapping. The Bell state fidelity is $0.9983^{+0.0008}_{-0.0035}$ before correcting for the state initialization error described above. Correcting for the initialization error of $3.5(2) \times 10^{-3}$, whose uncertainty is determined by bootstrapping the reference data, yields a corrected Bell state fidelity of $1^{+0}_{-0.0017}$. For the antisymmetric Bell state data, the population is $0.9967^{+0.0009}_{-0.0013}$ and the parity is $-0.9937^{+0.0020}_{-0.0019}$, giving an uncorrected Bell state fidelity of $0.9952^{+0.0010}_{-0.0013}$. Correcting for the state initialization error of $1.7(2) \times 10^{-3}$, we obtain a Bell state fidelity of $0.9977^{+0.0010}_{-0.0013}$.

E. Dataset selection

The data were taken before the detailed fidelity analysis tools presented in this manuscript were developed, so the experimental parameters were adjusted using less accurate fidelity estimation techniques to guide the optimization. Because of the inability to characterize and compensate for very small infidelities on the fly, the data were taken while sweeping experimental parameters (pulse durations and amplitudes/frequencies of control signals) through a range of values near the predicted optimum. As a result, some of the datasets were taken with nonoptimal parameters and should have lower-than-optimal underlying Bell state fidelity, but there is not an a priori method of knowing which datasets are which. Furthermore, drifts in both the motional frequency and the qubit frequency can cause nonmonotonic variation in the underlying Bell state fidelity due to effects related to the specific parameters of the shaped pulse rise and fall profiles[57]. There may also be other uncharacterized system parameters whose drifts cause fluctuations in the underlying Bell state fidelity, despite performing the entangling interaction with nominally identical parameters. In addition to any variation in underlying Bell state fidelity, there is statistical uncertainty (and thus dataset-to-dataset variation) in estimating the underlying Bell state fidelity. Each set of entanglement data took roughly 7 minutes to acquire.

As a result, we cannot a priori determine a single dataset or set of datasets that are anticipated to represent the best underlying Bell state fidelity. In order to avoid selection bias in determining which datasets to report as our best dataset, we use independent "trigger" data. We divide every set of experimental data, which includes both the parity and population measurements, in half, as described in Section III B. We use one half of the data as the "trigger," and report the fidelity of the other "analysis" half of the dataset with the highest "trigger" fidelity. Crucially, the "trigger" data are only used to select which dataset's "analysis" half to report; they are not used when calculating the fidelity of the "analysis" half. The "trigger" and "analysis" fidelities from the datasets, for both the symmetric and antisymmetric entangled states, are shown in Fig. S4.

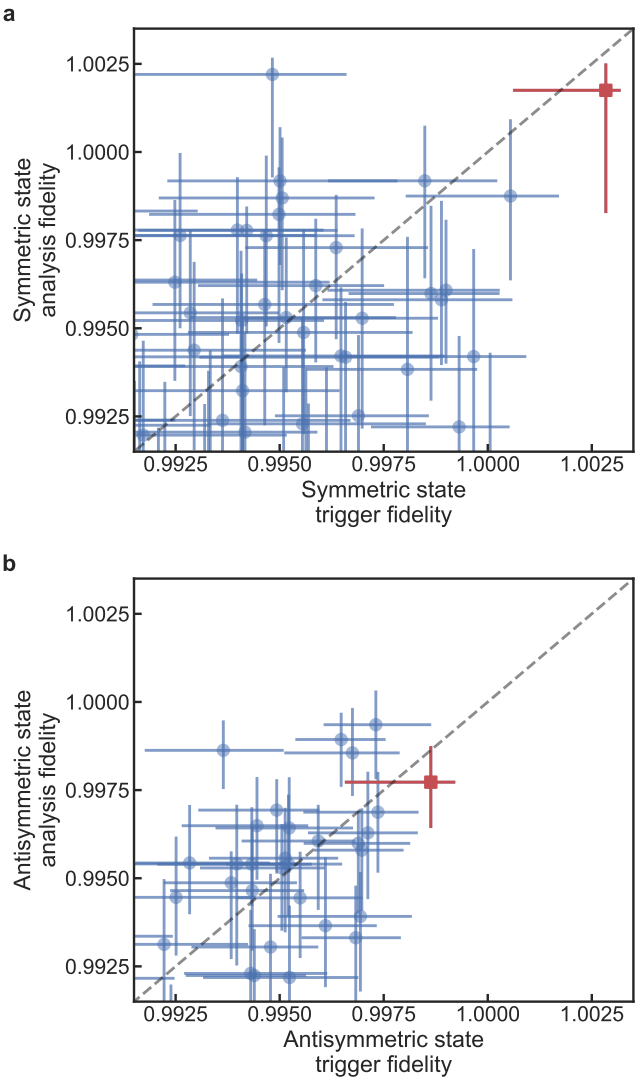

FIG. S4. **"Trigger" fidelities.** We use a "trigger" to select both the symmetric (**a**) and antisymmetric (**b**) entangled state data to report. For each set of data, we split each of our datasets into two. We use half to compute a "trigger" fidelity, and the other half to analyze the fidelity of the created state. We use the dataset with the highest trigger fidelity. The data used to determine the trigger fidelity are subsequently discarded and are not used to compute the gate fidelity. This process avoids relevant selection bias in choosing which fidelity to report. The red square denotes the dataset with the highest trigger value which we report in the main text. The error bars are determined by nonparametric bootstrapping, indicating the 68% confidence interval. Dashed lines indicate a slope of 1. Some datasets with lower trigger and/or analysis fidelities are not visible in these figures.

F. Linear estimator

We also use an unbiased linear estimator of Bell-state fidelity as a consistency check, implementing techniques similar to the linear estimation of process fidelity in Ref. 63 and the linear state tomography described in Ref. 64 that have been adapted for this analysis.

For an abstract experiment consisting of j different positive operator-valued measure (POVM) measurements $\{\Pi_i^{(j)}\}$ of an unknown state ρ, a linear estimator of the fidelity of ρ with a target state $|\psi\rangle\langle\psi|$ can be constructed from any decomposition of $|\psi\rangle\langle\psi|$ into a linear combination of the POVM elements $\{\Pi_i^{(j)}\}$. Such a decomposition is described by a set of real coefficients $\alpha_i^{(j)}$ that satisfy

$$|\psi\rangle\langle\psi| = \sum_i \sum_j \alpha_i^{(j)} \Pi_i^{(j)}. \tag{S8}$$

In this specific experiment, the different POVM measurements indexed by j correspond to the different collective rotations applied to the state before measurement. For each fixed j, the ith POVM element represents the measurement outcome associated to the observation of i photons during the measurement. The POVMs satisfy the standard normalization $\sum_i \Pi_i^{(j)} = 1$ for each j.

If all the probabilities $p_i^{(j)} = \mathrm{Tr}[\rho \cdot \Pi_i^{(j)}]$ of observing each POVM outcome were known exactly, the fidelity $F = \mathrm{Tr}[\rho \cdot |\psi\rangle\langle\psi|]$ could be computed using the decomposition in Eq. S8 according to

$$F = \sum_i \sum_j \alpha_i^{(j)} p_i^{(j)}. \tag{S9}$$

This observation motivates the construction of the linear estimator

$$\hat{F} = \sum_i \sum_j \alpha_i^{(j)} \frac{C_i^{(j)}}{n^{(j)}}, \tag{S10}$$

where $n^{(j)}$ is the number of times the jth POVM measurement is made during the experiment and $C_i^{(j)}$ is the random variable for the number of times the ith outcome is observed during those measurements.

For each j, the $C_i^{(j)}$ are distributed multinomially with $n^{(j)}$ trials and probabilities $p_i^{(j)} = \mathrm{Tr}[\rho \cdot \Pi_i^{(j)}]$, so the expected value of $\hat{F}$ is

$$\langle \hat{F} \rangle = \sum_i \sum_j \alpha_i^{(j)} \frac{n^{(j)}}{n^{(j)}} \mathrm{Tr}[\rho \cdot \Pi_i^{(j)}] = \mathrm{Tr}[\rho \cdot |\psi\rangle\langle\psi|], \tag{S11}$$

which shows $\hat{F}$ is an unbiased estimator of fidelity. The j runs are independent given ρ, so the variance of $\hat{F}$ is

$$\begin{aligned} \mathrm{Var}(\hat{F}) &= \sum_j \sum_{i,i'} \frac{\alpha_i^{(j)} \alpha_{i'}^{(j)}}{(n^{(j)})^2} \mathrm{Cov}(C_i, C_{i'}) \\ &= \sum_j \sum_{i,i'} \frac{\alpha_i^{(j)} \alpha_{i'}^{(j)}}{(n^{(j)})^2} n^{(j)} \left(p_i^{(j)} \delta_{ii'} - p_i^{(j)} p_{i'}^{(j)} \right), \end{aligned} \tag{S12}$$

again using the fact the C_i are multinomially distributed according to probabilities $p_i^{(j)}$.

Because the only constraints on the coefficients $\alpha_i^{(j)}$ are that they satisfy Eq. S8, an optimal choice of coefficients can be made that minimizes the variance of $\hat{F}$. After choosing to optimize near the reference state $|\psi\rangle\langle\psi|$ and plugging in $p_i^{(j)} = \mathrm{Tr}[\Pi_i^{(j)} \cdot |\psi\rangle\langle\psi|]$, the optimal coefficients can be found by solving a quadratic program.

In this experiment, the state space is modeled as a two-qutrit space where each ion has a computational-qubit subspace and a leaked state. The POVM elements are computed numerically assuming particular values of the Poissonian means and depumping and repumping rates calibrated from the reference data. For the purposes of the linear estimator, the fidelity is defined to be $\mathrm{Tr}[\rho \cdot |\psi\rangle\langle\psi|]$ where all the operators are on the full two-qutrit state space. The initialization-corrected fidelity is computed afterward by assuming a known leakage parameter.

Because of the assumptions about leakage, the constraints on the $\alpha_i^{(j)}$ in Eq. S8 become

$$\begin{aligned}\sum \alpha_i^{(j)}\Pi_i^{(j)} = &|\psi\rangle\langle\psi| \\ &+ A\big(|\uparrow a\rangle\langle\uparrow a| + |a\uparrow\rangle\langle a\uparrow|\big) \\ &+ B\big(|\downarrow a\rangle\langle\downarrow a| + |a\downarrow\rangle\langle a\downarrow|\big) \\ &+ C\big(|aa\rangle\langle aa|\big),\end{aligned} \tag{S13}$$

for real coefficients A,B,C that are left as free parameters during the optimization. Now, the associated estimator has an expectation value

$$\begin{aligned}&\mathrm{Tr}[\rho \cdot |\psi\rangle\langle\psi|] \\ &+ A\mathrm{Tr}[\rho \cdot (|\uparrow a\rangle\langle\uparrow a| + |a\uparrow\rangle\langle a\uparrow|)] \\ &+ B\mathrm{Tr}[\rho \cdot (|\downarrow a\rangle\langle\downarrow a| + |a\downarrow\rangle\langle a\downarrow|)] \\ &+ C\mathrm{Tr}[\rho \cdot (|aa\rangle\langle aa|)],\end{aligned} \tag{S14}$$

which is shifted from the fidelity by the last three terms. Using the assumptions about leakage and the values of A,B,C returned by the numerical optimization, those terms can be evaluated and subtracted off to recover an unbiased estimate of fidelity. For example, the symmetric entangled state is assumed to satisfy

$$\mathrm{Tr}[\rho \cdot (|\uparrow a\rangle\langle\uparrow a| + |a\uparrow\rangle\langle a\uparrow|)] = 2\epsilon(1-\epsilon), \tag{S15}$$

$$\mathrm{Tr}[\rho \cdot (|\downarrow a\rangle\langle\downarrow a| + |a\downarrow\rangle\langle a\downarrow|)] = 0, \tag{S16}$$

$$\mathrm{Tr}[\rho \cdot (|aa\rangle\langle aa|)] = \epsilon^2, \tag{S17}$$

where ϵ is the leakage parameter.

Using this method as a crosscheck, we compare the corrected fidelities we obtain to those reported in the main text using the standard parity analysis method[44] in Table I and find good agreement between the methods. We use the same bootstrapping procedure to obtain the 68 % confidence intervals.

G. Fidelity analysis bias estimation

We created simulated data using QuTip[65] to validate our fidelity analysis for both the symmetric and antisymmetric entangled states[57]. We varied both the underlying fidelity of the states created due to gate errors as well as leakage errors. We used the simulations to verify that our analysis is either unbiased or underestimates the fidelity of the states we create as shown in Fig. S5. We find that the parity analysis method is in general more negatively biased (towards a lower fidelity than the true fidelity) compared to the linear estimator. More details of these simulations and their fidelity analysis can be found in Ref. 57.

IV. ESTIMATES FOR LEADING SOURCES OF ERROR

In this section, we discuss the main sources of error in our entangling operation, which are estimated using QuTip simulations. More details can be found in Ref. 57.

A. Motional dephasing

Frequency fluctuations of the motional frequency ω_r during the entangling operation will cause dephasing of the ion motion and give rise to an error in the resulting state. This dephasing can usually be measured by implementing a Ramsey experiment on the ion motion. However, this measurement is challenging given our motional frequency drifts and the limited two-ion trap lifetime. We instead use an analysis of the squeezing of the ion motion[66] to estimate this dephasing, giving a motional coherence time of about 64 ms. This dephasing results in an error of 5.8×10^{-4} in the entangled state fidelity.

B. Motional frequency drifts

The motional frequency ω_r can drift by several kHz over approximately 7 minutes, the time required to take an entangling operation dataset. This effect appears to be related to charging of the trap surface from the 280 nm light used for laser cooling. The motional frequency drift needs to be carefully tracked to achieve the highest fidelities. We perform calibration measurements of the motional frequency every few seconds, interleaved with sets of entangling operation trials, and implement a simple linear feedforward to track and predict the drifts in ω_r. The feedforward prediction, which is used to adjust the frequencies of the qubit control signals for the entangling operation experiment, can be compared after the fact with the record of measured motional frequencies. The mean of the difference between the prediction and the actual frequency is 3.4 Hz, with a standard deviation of ≈ 50 Hz. These motional frequency fluctuations give

State	Fidelity analysis method	Original data	68 % confidence interval	Mean	Median
$\|\downarrow\downarrow\rangle + i\,\|\uparrow\uparrow\rangle$	Parity	1	[0.9983, 1]	1	1
$\|\downarrow\downarrow\rangle + i\,\|\uparrow\uparrow\rangle$	Linear estimator	1	[0.9989, 1]	1	1
$\|\downarrow\uparrow\rangle - \|\uparrow\downarrow\rangle$	Parity	0.9977	[0.9964, 0.9987]	0.9976	0.9976
$\|\downarrow\uparrow\rangle - \|\uparrow\downarrow\rangle$	Linear estimator	0.9985	[0.9968, 1]	0.9985	0.9985

TABLE I. **Comparison of different fidelity analysis methods.** The confidence interval, means and medians are based on the bootstrap distribution. Values above 1 are truncated.

rise to an estimated infidelity of approximately 3×10^{-5} in the final Bell state. In our experiment, the feedforward adjusts the value of δ and keeps ω_g fixed. This may cause some additional reduction in fidelity at specific δ values based on their relation to the duration and shape of the rising and falling microwave pulse edges[41].

C. Motional heating

Finally, we analyze the effect of heating. The motional heating rate of the out-of-phase mode used for the gate is so low that we are unable to measure it precisely; however 1 quanta/s is a conservative upper limit based on measurements. This heating rate will result in an error of 3×10^{-5} in the entangled state fidelity.

[8] Harty, T. P. *et al.* High-Fidelity Preparation, Gates, Memory, and Readout of a Trapped-Ion Quantum Bit. *Phys. Rev. Lett.* **113**, 220501 (2014).

[31] Monroe, C., Meekhof, D. M., King, B. E., Itano, W. M. & Wineland, D. J. Demonstration of a Fundamental Quantum Logic Gate. *Phys. Rev. Lett.* **75**, 4714-4717 (1995).

[41] Sutherland, R. T. *et al.* Versatile laser-free trapped-ion entangling gates. *New J. Phys.* **21**, 033033 (2019).

[42] Hayes, D. *et al.* Coherent Error Suppression in Multiqubit Entangling Gates. *Phys. Rev. Lett.* **109**, 020503 (2012).

[43] Srinivas, R. *et al.* Trapped-Ion Spin-Motion Coupling with Microwaves and a Near-Motional Oscillating Magnetic Field Gradient. *Phys. Rev. Lett.* **122**, 163201 (2019).

[44] Sackett, C. A. *et al.* Experimental entanglement of four particles. *Nature* **404**, 256–259 (2000).

[56] Wang, P. *et al.* Single ion qubit with estimated coherence time exceeding one hour. *Nat. Commun.* **12**, 233 (2021).

[57] Srinivas, R. *Laser-free trapped-ion quantum logic with a radiofrequency magnetic field gradient.* Ph.D. thesis, University of Colorado, Boulder (2020).

[58] Roos, C. F. *et al.* Nonlinear coupling of continuous variables at the single quantum level. *Phys. Rev. A* **77**, 040302 (2008).

[59] Nie, X. R., Roos, C. F. & James, D. F. V. Theory of cross phase modulation for the vibrational modes of trapped ions. *Phys. Lett. A* **373**, 422–425 (2009).

[60] Warring, U. *et al.* Techniques for microwave near-field quantum control of trapped ions. *Phys. Rev. A* **87**, 013437 (2013).

[61] Bowler, R., Warring, U., Britton, J. W., Sawyer, B. C. & Amini, J. Arbitrary waveform generator for quantum information processing with trapped ions. *Rev. Sci. Instrum.* **84**, 033108 (2013).

[62] Efron, B. & Tibshirani, R. J. *An introduction to the bootstrap* (CRC Press, 1994).

[63] Wan, Y. *et al.* Quantum gate teleportation between separated qubits in a trapped-ion processor. *Science* **364**, 875 (2019).

[64] Zhu, H. Quantum state estimation with informationally overcomplete measurements. *Phys. Rev. A* **90**, 012115 (2014).

[65] Johansson, J. R., Nation, P. D. & Nori, F. QuTiP 2: A Python framework for the dynamics of open quantum systems. *Comput. Phys. Commun.* **184**, 1234–1240 (2013).

[66] Burd, S. C. *et al.* Quantum amplification of boson-mediated interactions. *Nat. Phys.* **17**, 898–902 (2021).

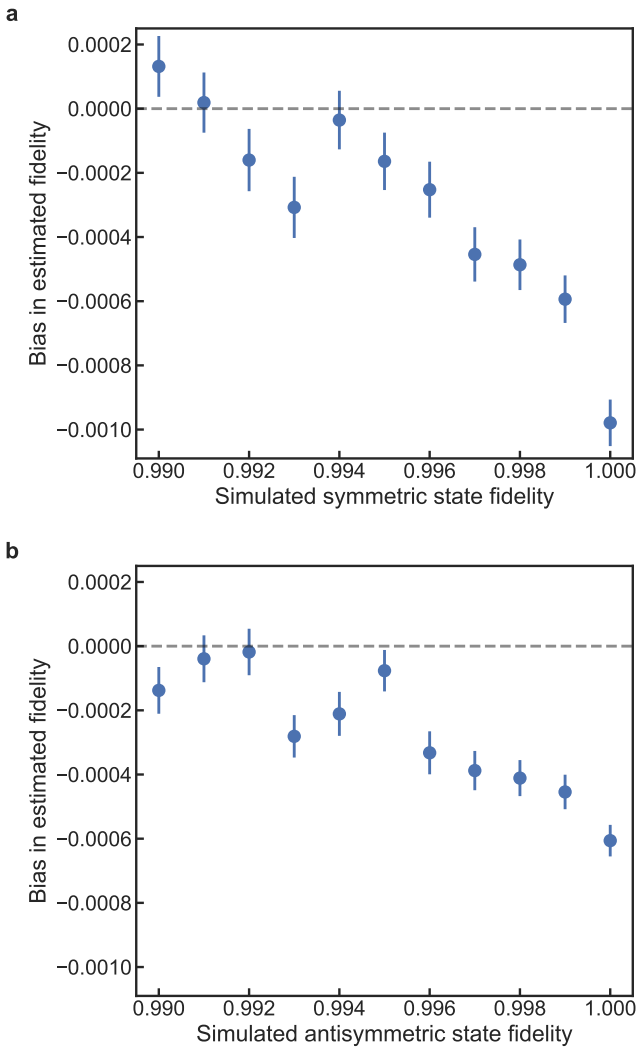

FIG. S5. **Bias in fidelity estimation.** We generate simulated data with identical statistics to the experiment, with different underlying fidelities for both the symmetric (**a**) and antisymmetric (**b**) entangled states. We plot the bias in estimated fidelity, the difference between the estimated fidelity and the simulated fidelity, for varying simulated fidelities. A negative bias corresponds to an estimated fidelity that is lower than the simulated fidelity. For each simulated fidelity, we generate 1000 sets of simulated data, including the effects of leakage with similar parameters to what was observed experimentally. For both symmetric and antisymmetric states, the simulated data were generated from a calculated density matrix for the final state at the end of the entangling operation. This density matrix was derived assuming that motional dephasing was the source of entangling gate infidelity. We see an overall negative bias in our estimated fidelity, whose magnitude increases as the underlying fidelity approaches 1.